Highly Organized Epitaxy of Dirac Semimetallic $PtTe_2$ Crystals with Extrahigh Conductivity and Visible Surface Plasmons at Edges

Lei Fu,[†,‡] Debo Hu,[∥] Rafael G. Mendes,[§] Mark H. Rümmeli,[§] Qing Dai,[∥] Bin Wu,[*,‡] Lei Fu,[*,†] and Yunqi Liu[*,‡]

[†]College of Chemistry and Molecular Science, Wuhan University, Wuhan 430072, People's Republic of China

[‡]Beijing National Laboratory for Molecular Sciences, Key Laboratory of Organic Solids, Institute of Chemistry, Chinese Academy of Sciences, Beijing 100190, People's Republic of China

[§]Soochow Institute for Energy and Materials InnovationS (SIEMIS), School of Energy Optoelectronics and Energy & Collaborative Innovation Center of Suzhou Nano Science and Technology, Soochow University, Suzhou 215006, People's Republic of China

[∥]National Center for Nanoscience and Technology, Beijing 100190, People's Republic of China

ABSTRACT: **Platinum telluride ($PtTe_2$), a member of metallic noble-transition-metal dichalcogenides (MNTMDs), has emerged as an indispensable candidate for superconducting, magnetic, and other electronic phase engineering, as well as optic applications. Herein, we report the van der Waals epitaxy of high-crystalline few-layer $PtTe_2$ crystals on inert mica. Density functional theory calculations are used to illustrate a type-II Dirac cone along the Γ-A direction in the $PtTe_2$ crystal. Impressively, the $PtTe_2$ devices exhibit an extra-high electrical conductivity of 10^7 S m^{-1}, 1000 times higher than that of metallic 1T MoS_2. Meanwhile, the magnetoresistance effect at low temperatures reaches 800% in a field of 9.0 T. Furthermore, near-field nanooptical properties are assessed on $PtTe_2$. Considering the subwavelength effect, the plasmonic wavelength $\lambda_p \approx 200$ nm of 1T $PtTe_2$ is obtained and the carrier concentration calculated from λ_p is about 1.22×10^{15} cm^{-2}, which is 100-fold higher than that of $MoTe_2$ in the previous reports. Therefore, our work demonstrates the growth of MNTMDs and provides insights into the plasmonic properties of 2D metallic telluride compounds.**

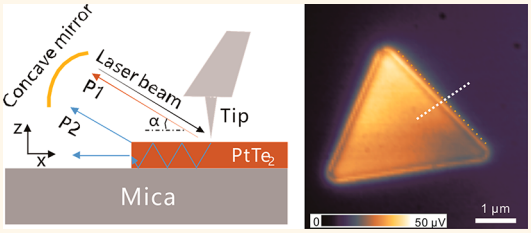

KEYWORDS: *Dirac semimetal, platinum telluride, van der Waals epitaxy, electrical conductivity, plasmons*

Two-dimensional transition metal dichalcogenides (TMDs), having the chemical formula MX_2 (where M = IVB−VIII metals and X = chalcogens), have attracted great attention in the past decade for their properties and potential applications in next-generation electronics, optoelectronics, and energy devices.[1−4] Meanwhile, 2D metallic transition metal dichalcogenides (MTMDs) are important metallic components for the fabrication of 2D van der Waals (vdW) heterostructures, which provides versatile applications by combining a wide range of 2D materials with different conductivity (*e.g.*, metals, semiconductors, and insulators).[5−8] Encouragingly, the PtX_2 (X = S, Se, Te) class is becoming one of the most promising functional materials among metallic noble-transition-metal dichalcogenide (MNTMD) materials.[9−15] The high room-temperature electron mobility and energy-gap tunability upon thickness reduction can be applied to build optoelectronic field-effect transistors.[9,12] Among the PtX_2 class, platinum telluride ($PtTe_2$) with the existence of type-II Dirac fermions has been predicted to be a promising candidate for catalysis and electronics.[13,14] $PtTe_2$ crystallizes in a triangular CdI_2 crystal structure. Six Te atoms surround the central Pt atom by constituting a $PtTe_6$ octahedral basal plane. Octahedrons are linked at edges to form an atomic plane. A strong interaction in chalcogen layers makes the p_z valence bands of chalcogen more dispersive, leading to the typical metallic behavior of $PtTe_2$.

Recently, Zhou and colleagues reported experimental evidence of the strongly inclined Dirac pyramids in the Γ-A direction, confirming type II Dirac fermions in bulk $PtTe_2$ crystals.[13] The studies indicate the need for exploring quantum effect and topological phase transitions. However, the detailed optical

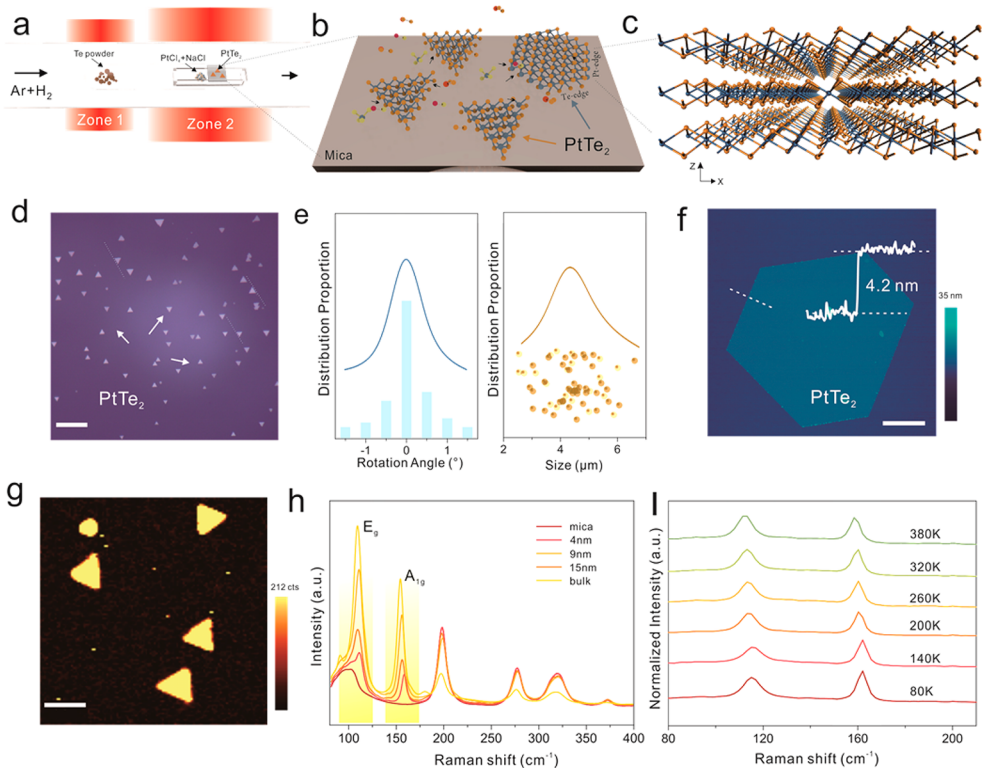

Figure 1. Synthesis and crystal structure of layered $PtTe_2$. (a) Schematic of the ambient-pressure CVD growth approach. (b) Surface reaction during the epitaxial growth process of $PtTe_2$ on mica. (c) Crystal structure of 1T $PtTe_2$. (d) Optical microscopy images of the $PtTe_2$ crystals on mica. Scale bar, 20 μm. (e) Statistical distributions of the rotation angles and crystal sizes. (f) The thickness of the $PtTe_2$ crystal is 4.2 nm from the AFM cross-sectional profile along the dotted line. Scale bar, 1 μm. (g) Raman mapping (A_{1g} mode) of a triangular $PtTe_2$ crystal. Scale bar, 5 μm. (h) Raman spectra of $PtTe_2$ with different thicknesses. (i) Temperature-dependent Raman spectra of $PtTe_2$, respectively.

and electronic properties of $PtTe_2$ nanoscale electronic devices have been studied sparsely, and to date, the direct synthesis of low-dimentional $PtTe_2$ has not been reported due to rare precursors available and difficulty in synthesis methods. Herein, we achieve vdW epitaxial growth of atomic layered metallic 1T $PtTe_2$ crystals on mica. Impressively, $PtTe_2$ devices exhibit an extra-high electrical conductivity of 10^7 S m^{-1}, 1000 times higher than that of metallic 1T MoS_2. Meanwhile, the magnetoresistance effect at low temperatures reaches 800% in a field of 9.0 T. Furthermore, near-field nanooptical properties are measured on $PtTe_2$ crystals. Considering the subwavelength effect, the plasmonic wavelength $\lambda_p \approx 200$ nm of 1T $PtTe_2$ could be obtained and a carrier concentration calculated from λ_p is about 1.22×10^{15} cm^{-2}, which is 100-fold higher than that of $MoTe_2$ in the previous reports. Therefore, our work demonstrates the growth of MNTMDs and provides insights into the plasmonic properties of 2D metallic telluride compounds.

RESULTS AND DISCUSSION

Chemical vapor deposition (CVD) techniques have been applied to produce various transition metal sulfide and selenide compounds.[16−18] However, due to the low chemical reactivity and the small electronegativity difference of Pt and Te, the CVD growth of stoichiometric ditellurides has been rarely reported. To achieve the growth of high-crystalline $PtTe_2$ crystals, we designed a salts-assisted evaporation strategy to maintain the continuous supply of Pt precursor, as seen in Figure 1a. Low-melting-point $PtCl_4$ was selected as a precursor, and stoichiometric NaCl used as a melting-assisting medium was employed in the sustained-evaporation process. $PtCl_4$ and NaCl could be well mixed in water, forming a homogeneous precursor of $PtCl_4$/NaCl after drying. When heated to a high temperature of 800 °C, the volatile source will coevaporate slowly and a chemical reaction will occur with Te powders and hydrogen (H_2 10 vol %) simultaneously.

The vdW epitaxy mode enables the epitaxial growth of TMDs even with large lattice mismatch and different crystalline symmetries.[19−21] At the same time, fluorophlogopite is considered to be an ideal epitaxial substrate because of its surface inertness and its relatively high thermal stability.[22] The small migration barriers of Pt and Te atoms on the mica substrate lead to the rapid lateral growth of 2D $PtTe_2$ crystals (Figure 1b).

As shown in Figure 1c, the atomic structure of $PtTe_2$ consists of three covalently bonded Te−Pt−Te atomic planes, and six Te atoms surround the central Pt atom with the crystal constants of $a = b = 4.09$ Å, as well as $c = 5.34$ Å.[13] The spacing between the layers is 0.59 nm, showing weak vdW interactions. $PtTe_2$ adopts the CdI_2 structure corresponding to space group $P\bar{3}m1$. Figure 1d shows an optical microscopy image of several $PtTe_2$ triangular crystals synthesized on the mica substrate. The edges of crystals on mica are oriented essentially at multiples of ~60° (Figure 1e). Meanwhile, rotating the $PtTe_2$ crystal lattice by 60° should contribute to the epitaxial growth of $PtTe_2$ on the mica. In addition, the inertness of the substrate may cause a statistically equivalent nucleation rate of $PtTe_2$, and the size of crystals is relatively uniform, so it is hopeful to prepare crystal arrays (Figure 1e). The representative atomic force microscopy (AFM) image with thicknesses of ~4.2 nm is displayed in Figure 1f.

The Raman spectra of $PtTe_2$ crystals of different thicknesses were studied with a 532 nm excitation laser in Figure 1h. The

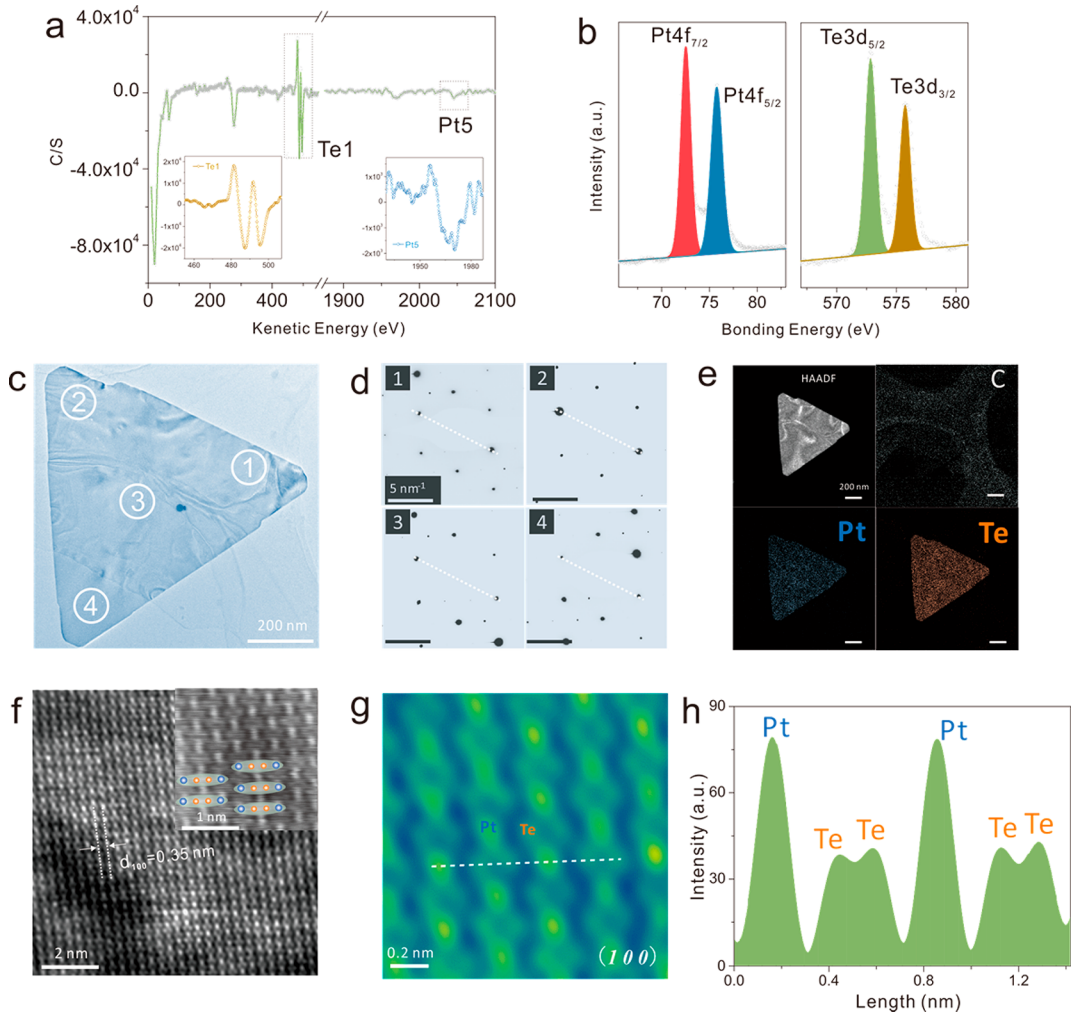

Figure 2. Chemical compositions and atomic structure of the synthesized $PtTe_2$ crystals. (a) Auger electron spectrum of a grown 2D $PtTe_2$ crystal. (b) XPS analysis of as-synthesized $PtTe_2$ crystals. On the left is the Pt 4f state assigned with two peaks, while on the right is the Te 3d state. (c) Low-magnification ADF-STEM image of a $PtTe_2$ crystal. (d) SAED pattern from the selected area of the crystal; SAED patterns taken from the areas labeled with numbers 1−4 in (c). The angles of the dashed lines with respect to the horizontal line were labeled in the patterns. (e) EDS elemental mapping of C-K, Pt-M, and Te-L of a $PtTe_2$ crystal, respectively. (f) Atomic-resolution HAADF-STEM image (filtered) of the $PtTe_2$ crystal. (g) False-color coded according to the HAADF intensity of the inset in (f). The positions of the Pt and Te atoms are colored yellow and green, respectively. (h) Intensity line profle with the same color-coding method along the white dashed line in (g).

110.7 cm^{-1} peak matches up to the E_g mode from the in-plane Te−Pt−Te lattice vibrational mode, and the 158.2 cm^{-1} one matches up to the A_{1g} mode from the out-of-plane vibrational mode.[13] As the thickness increases, the Raman intensity increases obviously due to the increase of scattering centers in the $PtTe_2$ crystals. The A_{1g} mode peak intensity map of triangular $PtTe_2$ crystals is given in Figure 1g, indicating the uniform crystallinity of the $PtTe_2$ crystals. Temperature-dependent Raman spectroscopy is widely used to characterize the anharmonic lattice vibrations.[23] Herein, representative Raman spectra of $PtTe_2$ were measured from 80 to 380 K. Obviously, both A_{1g} and E_g modes soften and red shift as the temperature increases (Figure 1i). We extract the linear temperature coefficients (X) from the slopes of E_g and A_{1g} modes in $PtTe_2$, which are −0.015 and −0.012 cm^{-1} K^{-1}, respectively (Figure S1).

In order to exclude possible Na or Cl element residues in $PtTe_2$ crystals, we measured $PtTe_2$ crystals using nano-Auger electron spectroscopy (AES). No Na or Cl element was measured by AES, and the atomic ratio of Te:Pt was ∼2.03, consistent with the stoichiometric ratio of $PtTe_2$ (Figure 2a). Figure 2b shows two distinct peaks at 72.6 and 75.8 eV attributed to the Pt $4f_{7/2}$ and Pt $4f_{5/2}$ states in X-ray photoelectron spectroscopy (XPS) characterization, respectively. Similarly, two peaks at 572.8 and 575.7 eV represent the Te $3d_{5/2}$ and Te $3d_{3/2}$ states, corresponding to the values of $PtTe_2$ in the NIST X-ray Photoelectron Spectroscopy Database.

The chemical compositions and atomic structures of the synthesized $PtTe_2$ crystals are further revealed by atom-resolved scanning transmission electron microscopy (STEM) imaging, selected-area electron diffraction (SAED), and energy-dispersive X-ray spectroscopy (EDS). Figure 2c shows the low-magnification TEM image of a $PtTe_2$ sample. The SAED patterns recorded from four different regions show the perfect coincidence, confirming its single-crystal nature (Figure 2d). EDS was used to identify the chemical constituents of as-grown layers. The EDS mapping characterizations display the homogeneous spatial distribution of the Te element and Pt element in Figure 2e. The full spectrum of EDS reveals the atomic ratio of Te to Pt is 65.6 to 32.7, matching the stoichiometric ratio of $PtTe_2$ (Figure S2).

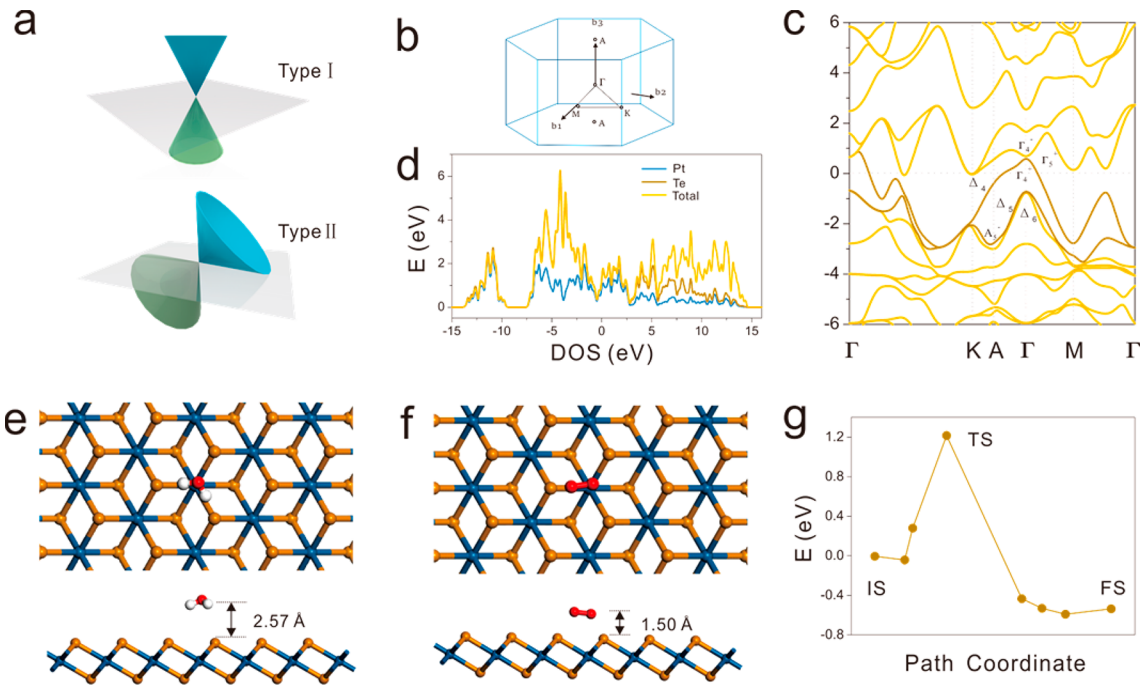

Figure 3. Theoretical calculation of type-II Dirac $PtTe_2$. (a) Schematic drawing of type-II Dirac fermions. (b) Projected surface Brillouin zone. (c) Calculated band dispersion along the in-plane Γ-K-Γ-M direction. (d) Projected density of states of $PtTe_2$. (e) Configurations of the physisorbed H_2O on $PtTe_2$. (f) Configurations of the physisorbed initial state of O_2 on $PtTe_2$. (g) Energy profile of the reaction pathway for O_2 on $PtTe_2$.

Figure 2f shows a high-resolution Z-contrast STEM image of a $PtTe_2$ crystal, revealing that from the top view six Te atoms surround the central Pt atom, implying the octahedral structure in the 1T phase. It is well known that the contrast of a HAADF-STEM image is approximately equal to the atomic number *Z*. In view of this, the Pt atoms are the brightest ones and the two stacked Te atoms are the dimmest ones. Six Te atoms surround the central Pt atom with interplanar crystal spacing of 3.5 Å, corresponding to the (100) planes of $PtTe_2$. A false-color coded image by the HAADF intensity of the inset region in Figure 2f is presented with the Pt and Te atoms colored yellow and green, respectively (Figure 2g). As shown in Figure 2h, the in-plane lattice constant of the crystal is measured as ∼0.35 nm by the intensity profile along the white line in Figure 2g. As is well known, the folded edge of TMDs could be used to identify the layer spacing *d* in TEM characterizations. As displayed in Figure S3, the *d* spacing of the $PtTe_2$ crystal was measured to be ∼0.59 nm along the white arrow. Briefly, the systematic STEM characterizations confirm that well-shaped $PtTe_2$ crystals are highly crystalline in the 1T-phase structure (Figure S4).

In order to reveal the topological type-II Dirac nature (see schematic drawing in Figure 3a) and air stability of the $PtTe_2$ crystals at room temperature, we have performed calculations in the framework of density functional theory (DFT) with periodic-edge conditions. Figure 3b shows the band structure calculated along the direction of K-A-Γ-M through the Γ point. Since the band inversion is between Γ_4^+ and Γ_4^-, the topologically nontrivial gap results in the surface states of the gapped cone structure. The Dirac cone consists of two Te-p valence bands (deep color) (Figure 3c,d). The band crossing appears because the two bands correspond to different irreducible representations (Δ_4 and Δ_{5+6}), which prohibit hybridization between each other. Meanwhile, both hole and electron pockets coexist at the Fermi surface, suggesting the semimetallic characteristics of the material. In addition, DFT calculations are further applied to study air stability of $PtTe_2$. As shown in Figure 3e,f, both O_2 and H_2O tend toward physisorption, and the maximum adsorption energies are 0.06 and 0.53 eV, which may not significantly change the electronic structures of $PtTe_2$. Besides physisorption, the dissociative adsorption reaction[24,25] of H_2O is an endothermic reaction adsorbing 2.83 eV, which is disadvantageous from an energetics point of view. Apart from this, it should be noted that the dissociative reaction of O_2 on $PtTe_2$ is an endothermic reaction releasing 0.53 eV. But our calculations show that a high dissociative reaction barrier of 1.22 eV exists, so it may not be oxidized significantly at room temperature (Figure 3g).

Temperature-dependent transport measurements were used to investigate the electrical properties of the synthesized $PtTe_2$ crystals. The temperature dependence of the resistivity of $PtTe_2$ crystals on different thicknesses is illustrated in Figure 4a. For the 9 nm device, the room-temperature resistance is 5.81 Ω and decreases to 0.34 Ω at 2 K, yielding a residual resistivity ratio of ∼17 (Figure 4a,b). In addition, the relatively high conductivity at 300 K of the 9 nm $PtTe_2$ is about 6.4×10^6 S m^{-1}, approximately 3 orders of magnitude higher than that for metallic 1T MoS_2.[26] It can be noticed that at above 50 K the electrical resistivity decreases monotonically with decreasing temperature, indicating the metallic behavior of the $PtTe_2$ crystals and the electron−phonon scattering dominant mechanism in this temperature range. Meanwhile, a plateau in the curve was observed as *T* further reduces (Figures 4a, S5). This phenomenon may result from the 2D electron−electron interactions at the reduced dimension of few-layer $PtTe_2$ crystal.[27] As shown in Figure 4c, various magnetic fields were applied to study the temperature-dependent resistivity. When a field is applied, the resistivity curve basically follows the zero-field curve until the temperature decreases to 80 K, below which the curve begins to rise

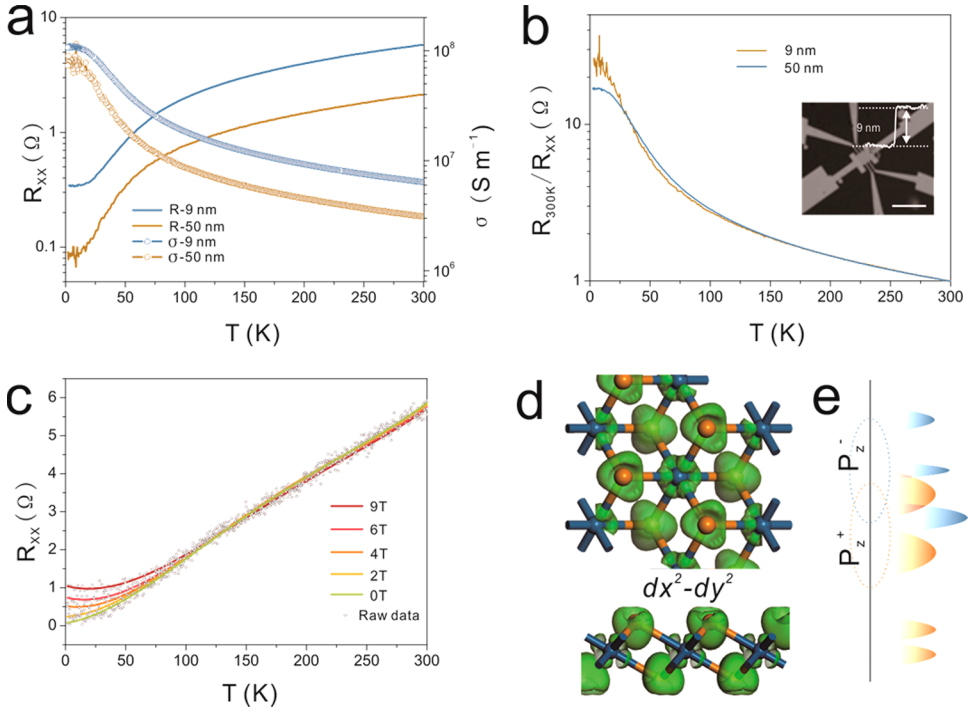

Figure 4. Electrical transport properties of ultrathin metallic $PtTe_2$. (a) Temperature dependence of the resistivity (left) and electrical conductivity (right) for the $PtTe_2$ devices. (b) Temperature dependence of the $R_{300\ K}/R_{xx}$ of $PtTe_2$ with different thicknesses. Inset: Typical Hall bar device fabricated with a 9 nm $PtTe_2$ crystal. (c) Temperature and field dependence of the magnetoresistance in $PtTe_2$ with a thickness of 9 nm. (d) Visualized wave functions of the CBM state in $PtTe_2$. (e) Schematic of the density of electronic states for $PtTe_2$. Orange curves represent chalcogen bands, and blue curves represent metal bands.

obviously. The magnetoresistance effect reaches 800% at 2.2 K in a 9.0 T magnetic field. As a larger field is applied, the "fork lift" temperature is shifted to a higher value, implying that there exists a competition between dominating scattering mechanisms.

Such high conductivity of $PtTe_2$ partially results from the small deformation potential of $PtTe_2$, representing electron−phonon scattering strength. The smaller deformation potential in $PtTe_2$ is launched in the isolated wave function around the conduction band minimum (CBM) ($d_{x^2-y^2}$ orbital of Pt atoms) in Figure 4d. Meanwhile, a strong interaction in chalcogen layers makes the p_z valence bands of the chalcogen more dispersive. The p_z^- band could merge the energy gap, ensuring that $PtTe_2$ is a semimetal with relatively high conductivity (Figure 4e).[28]

The circumnavigation of free electrons and long-range Coulomb interactions in semimetals make it possible to create surface plasmons. Therefore, if the excitation wave vector matches the plasmon polaritons, surface plasmon waves in the thin $PtTe_2$ crystals can be excited. Here, a scattering-type scanning near-field optical microscope (s-SNOM) was applied to observe propagating plasmons, similar to the previous reports of graphene plasmons.[29,30] As shown in Figure 5a, a schematic diagram generally describes the scanning plasmon interferometry technique. The AFM metallized tip illuminated by an infrared light generates a "lightning-rod" effect with a strong localized field around the tip apex.[31] The AFM topography map shows a smooth $PtTe_2$ surface free of wrinkles or defects with a height of ∼8 nm (Figure 5b). The IR nanoscopic image was obtained simultaneously under the excitation frequency of 920 cm^{-1} in Figure 5c. The fringes parallel to the edge direction are observed in the near-field images, resulting from the interference between circular plasma waves launched from the tip and image waves reflected from the $PtTe_2$ edge. The plasmon propagation can be described by $s(x) = A\frac{e^{i2xq_p}}{\sqrt{x}} + B\frac{e^{ixq_p}}{x^a}$, in which A and B are fitting parameters and q_p is a plasmonic wavevector. The first part is the circular wave launched from the tip, which propagates radially and reflects from the $PtTe_2$ edge with a propagating distance of $2x$. The second part is plane wave launched from the edge with a propagating distance of x, which is much weaker than the tip-launching plasmons. Because the plasmons return to the tip after propagating a $2x$ distance, the spacing between fringes is $\lambda_p/2$. An obvious peak appearing in the derivative signals at the momentum $q_p = 1/\lambda_p \approx 5 \times 10^6\ m^{-1}$ was extracted from the Fourier analysis profile in q-space (the inset of Figure 5d). Meanwhile, the result is confirmed by fitting with the interference function $s(x) = A(0) + e^{-ix}B\sin[\pi(x - C)/D]$, as shown in Figure 5d. Based on excitation frequency and q_p, the in-plane optical conductivity of $PtTe_2$ $\sigma(\omega)$ can be derived from the dispersion 2D free carriers model on a dielectric substrate,[32] which is $\frac{\varepsilon_1}{\sqrt{q^2 - \frac{\varepsilon_1\omega^2}{c^2}}} + \frac{\varepsilon_2}{\sqrt{q^2 - \frac{\varepsilon_2\omega^2}{c^2}}} = -\frac{i\sigma}{\varepsilon_0\omega}$, where ε_1 and ε_2 are the dielectric constant of air and substrate and q and ω are the momentum and excitation frequency. Meanwhile, the Drude model could describe its conductivity with $\sigma(\omega) = i\frac{ne2/m}{\omega + i\tau^{-1}}$, in which m is the effective mass of carriers, n is the carrier concentration, and τ is the relaxation time, respectively. Given an effective mass of $m = 0.9m_0$ (m_0 is the free electron mass) in $PtTe_2$,[33] a carrier concentration of about $1.22 \times 10^{15}\ cm^{-2}$ could be obtained, which is 100-fold higher than that of 1T $MoTe_2$ in the previous reports.[34] In Figure 5e−f, we display the selected s-SNOM images of a 11 nm (Figure S6) $PtTe_2$ planar waveguide at various excitation frequencies. The interference fringes are observed clearly on $PtTe_2$ parallel to the edges (dashed lines), and the fringes show an excitation frequency dependence. The

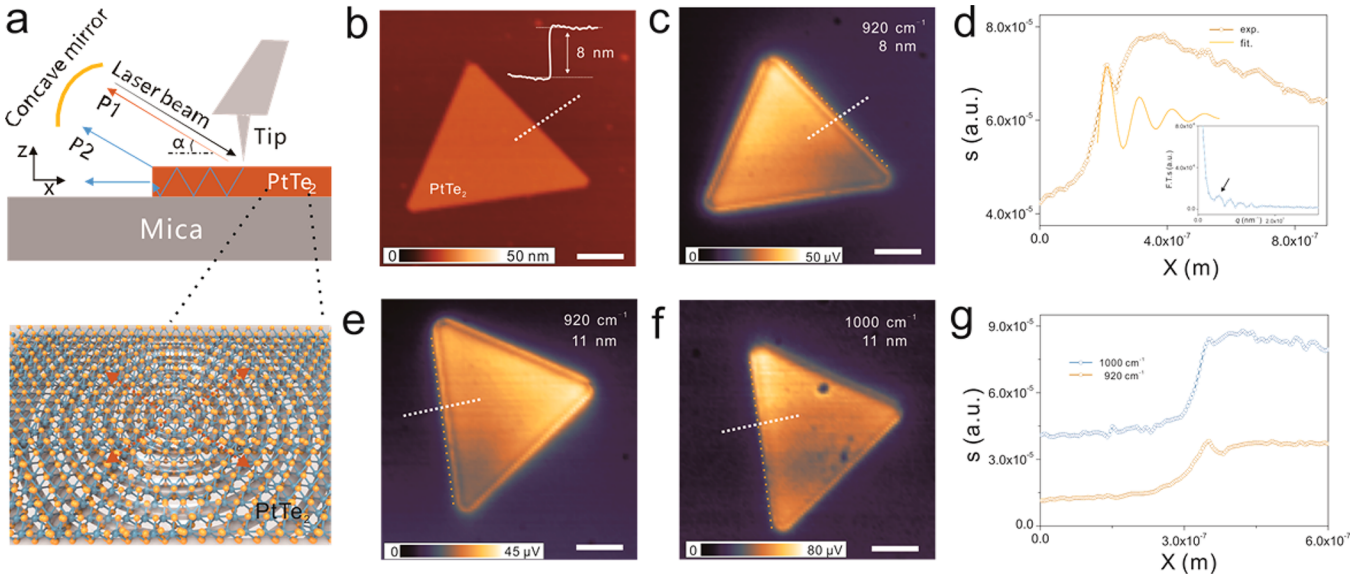

Figure 5. Nanooptical imaging of a $PtTe_2$ planar waveguide. (a) Schematic of concentric waveguide modes in $PtTe_2$ launched by the laser-illuminated s-SNOM tip. (b) AFM topographic image of 8 nm $PtTe_2$. (c) Concurrently acquired nanooptical imaging data with an excitation frequency of 920 cm^{-1}. The edge of the $PtTe_2$ crystal is marked by the orange dashed line. (d) Cross-sectional profile obtained from (b) across the fringes on $PtTe_2$ along the white dashed line; the yellow line is the fitting result. Inset: Fourier analysis momentum (q) profile of a $PtTe_2$ surface plasma wave at an excitation frequency of 920 cm^{-1} in q-space. (e, f) Selected s-SNOM imaging data of an 11-nm-thick $PtTe_2$ planar waveguide taken at various excitation frequencies. (g) Cross-sectional profile obtained from (e) and (f). The orange dashed lines mark the sample edge. Scale bars, 1 μm.

fringe shows a higher intensity as the excitation frequency decreases, and the fringes extend further into $PtTe_2$ at lower excitation frequency. Based on the above, it is worth further exploring polarizable surface-metallic characteristics and functionalities by patterning photonic structures on TMD crystals.

CONCLUSION

In summary, we designed a salts-assisted evaporation strategy to achieve the vdW epitaxial growth of highly crystalline atomic layered $PtTe_2$ crystals on mica. DFT calculations are applied to elucidate the type-II Dirac cone along the Γ-A direction in the $PtTe_2$ crystal. Impressively, the devices exhibit an excellent extra-high electrical conductivity of 10^7 S m^{-1}, 1000 times higher than that of metallic 1T MoS_2. Meanwhile, the magnetoresistance effect at low temperatures reaches 800% in a field of 9.0 T. Furthermore, the subwavelength effects of 1T-phase $PtTe_2$ are first observed by near-field nanooptical imaging. The plasmonic wavelength $\lambda_p \approx 200$ nm of 1T $PtTe_2$ is obtained, and a carrier concentration calculated from λ_p is about 1.22×10^{15} cm^{-2}, which is 100-fold higher than that of $MoTe_2$ in previous reports. Therefore, our work demonstrates the growth of MNTMDs and provides insights into the plasmonic properties of 2D metallic telluride compounds.

METHODS

Direct CVD Growth of $PtTe_2$ Crystals. We used Te powder (>99.98%, Sigma-Aldrich), $PtCl_4$ (>99.9%, Aladdin), and NaCl (>99.9%, Aladdin) as reaction sources. First, the 40 mg mixture of $PtCl_4$ and NaCl with the mass ratio of 1:3 was dissolved in 10 mL of deionized water. The $PtCl_4$/NaCl solution was heated at 250 °C for 30 min to remove the water. Te powder (60 mg) was placed upstream, 8 cm away from a mica substrate in a quartz tube. Before heating, the whole quartz tube was evacuated to 50 mTorr, then filled with Ar (99.999% purity), and the whole process was repeated three times. Then, the furnace temperature was raised to 800 °C for 30 min in a carrier gas with a hydrogen to argon ratio of 1:10 for the growth of $PtTe_2$. When the growth ends, a 500 sccm Ar flow was used to remove residual reactants from the tube, and the reaction zone was rapidly cooled to room temperature.

Device Fabrication. The $PtTe_2$ crystals were transferred to a 285 nm SiO_2/Si substrate with poly(methyl methacrylate) assistance. The devices were fabricated by e-beam lithography and thermal evaporation with electrodes made of 5 nm Ti and 100 nm Au. Electrical characterizations were performed with a physical property measurement system by Quantum Design.

Characterization. Raman spectroscopy was taken with a Renishaw instrument, and the AFM images were carried out using a Veeco Nanoscope. The TEM characterizations were performed with FEI Titan G2. The nanoimaging experiments were carried out using a commercial s-SNOM at the wavenumber of 920 or 1000 cm^{-1}.

ASSOCIATED CONTENT

Supporting Information

The Supporting Information is available free of charge

Corresponding linear temperature coefficients (X) of E_g and A_{1g} Raman modes plotted as the experimental temperature; TEM-EDS survey spectrum of the $PtTe_2$; $dR/dT-T$ curves of a 9 nm $PtTe_2$ crystal device; AFM topographic image of a 11 nm $PtTe_2$ crystal (PDF)

AUTHOR INFORMATION

Corresponding Authors

*E-mail: wubin@iccas.ac.cn.
*E-mail: leifu@whu.edu.cn.
*E-mail: liuyq@iccas.ac.cn.

ORCID

Lei Fu: 0000-0003-1356-4422
Yunqi Liu: 0000-0001-5521-2316

Notes

The authors declare no competing financial interest.

ACKNOWLEDGMENTS

The authors acknowledge support from Grant No. 2016YFA0200101, the National Natural Science Foundation of China (Nos. 21633012, 61390500, 51233006, and 60911130231), Beijing Municipal Science and Technology Commission (No. Z161100002116025), and the Chinese Academy of Sciences (No. XDB12030100).

REFERENCES

(1) Bonaccorso, F.; Colombo, L.; Yu, G. H.; Stoller, M.; Tozzini, V.; Ferrari, A. C.; Ruoff, R. S.; Pellegrini, V. Graphene, Related Two-Dimensional Crystals, and Hybrid Systems for Energy Conversion and Storage. *Science* **2015**, *347*, 1246501.

(2) Koppens, F. H. L.; Mueller, T.; Avouris, P.; Ferrari, A. C.; Vitiello, M. S.; Polini, M. Photodetectors Based on Graphene, Other Two-Dimensional Materials and Hybrid Systems. *Nat. Nanotechnol.* **2014**, *9*, 780−793.

(3) Georgakilas, V.; Perman, J. A.; Tucek, J.; Zboril, R. Broad Family of Carbon Nanoallotropes: Classification, Chemistry, and Applications of Fullerenes, Carbon Dots, Nanotubes, Graphene, Nanodiamonds, and Combined Superstructures. *Chem. Rev.* **2015**, *115*, 4744−4822.

(4) Cho, S.; Kim, S.; Kim, J. H.; Zhao, J.; Seok, J.; Keum, D. H.; Baik, J.; Choe, D. H.; Chang, K. J.; Suenaga, K.; Kim, S. W.; Lee, Y. H.; Yang, H. Phase Patterning for Ohmic Homojunction Contact in $MoTe_2$. *Science* **2015**, *349*, 625−628.

(5) Liu, Y.; Weiss, N. O.; Duan, X.; Cheng, H. C.; Huang, Y.; Duan, X. F. Van Der Waals Heterostructures and Devices. *Nat. Rev. Mater.* **2016**, *1*, 16042.

(6) Duan, X.; Wang, C.; Shaw, J. C.; Cheng, R.; Chen, Y.; Li, H.; Wu, X.; Tang, Y.; Zhang, Q.; Pan, A. L.; Jiang, J.; Yu, R.; Huang, Y.; Duan, X. F. Lateral Epitaxial Growth of Two-Dimensional Layered Semiconductor Heterojunctions. *Nat. Nanotechnol.* **2014**, *9*, 1024−1030.

(7) Xu, K.; Chen, P.; Li, X.; Wu, C.; Guo, Y.; Zhao, J.; Wu, X.; Xie, Y. Ultrathin Nanosheets of Vanadium Diselenide: A Metallic Two-Dimensional Material with Ferromagnetic Charge-Density-Wave Behavior. *Angew. Chem., Int. Ed.* **2013**, *52*, 10477−10481.

(8) Wang, J.; Zheng, H.; Xu, G.; Sun, L.; Hu, D.; Lu, Z.; Liu, L.; Zheng, J.; Tao, C.; Jiao, L. Y. Controlled Synthesis of Two-Dimensional 1T-$TiSe_2$ with Charge Density Wave Transition by Chemical Vapor Transport. *J. Am. Chem. Soc.* **2016**, *138*, 16216−16219.

(9) Zhao, Y. D.; Qiao, J. S.; Yu, Z. H.; Yu, P.; Xu, K.; Lau, S. P.; Zhou, W.; Liu, Z.; Wang, X. R.; Ji, W.; Chai, Y. High-Electron-Mobility and Air-Stable 2D Layered $PtSe_2$ FETs. *Adv. Mater.* **2017**, *29*, 1604230.

(10) Yim, C.; Lee, K.; McEvoy, N.; O'Brien, M.; Riazimehr, S.; Berner, N. C.; Cullen, C. P.; Kotakoski, J.; Meyer, J. C.; Lemme, M. C.; Duesberg, G. S. High-Performance Hybrid Electronic Devices from Layered $PtSe_2$ Films Grown at Low Temperature. *ACS Nano* **2016**, *10*, 9550−9558.

(11) Wang, Y. L.; Li, L. F.; Yao, W.; Song, S. R.; Sun, J. T.; Pan, J. B.; Ren, X.; Li, C.; Okunishi, E.; Wang, Y. Q.; Wang, E. Y.; Shao, Y.; Zhang, Y. Y.; Yang, H. T.; Schwier, E. F.; Iwasawa, H.; Shimada, K.; Taniguchi, M.; Cheng, Z. H.; Zhou, S. Y.; et al. Monolayer $PtSe_2$, a New Semiconducting Transition-Metal-Dichalcogenide, Epitaxially Grown by Direct Selenization of Pt. *Nano Lett.* **2015**, *15*, 4013−4018.

(12) Li, L.; Wang, W. K.; Chai, Y.; Li, H. Q.; Tian, M. L.; Zhai, T. Y. Few-Layered PtS_2 Phototransistor on h-BN with High Gain. *Adv. Funct. Mater.* **2017**, *27*, 1701011.

(13) Yan, M. Z.; Huang, H. Q.; Zhang, K. N.; Wang, E. Y.; Yao, W.; Deng, K.; Wan, G. L.; Zhang, H. Y.; Arita, M.; Yang, H. T.; Sun, Z.; Yang, H.; Wu, Y.; Fan, S. S.; Duan, W. H.; Zhou, S. Y. Lorentz-Violating Type-II Dirac Fermions in Transition Metal Dichalcogenide $PtTe_2$. *Nat. Commun.* **2017**, *8*, 257.

(14) Politano, A.; Chiarello, G.; Kuo, C. N.; Lue, C. S.; Edla, R.; Torelli, P.; Pellegrini, V.; Boukhvalov, D. W. Tailoring the Surface Chemical Reactivity of Transition-Metal Dichalcogenide $PtTe_2$ Crystals. *Adv. Funct. Mater.* **2018**, *28*, 1706504.

(15) Soluyanov, A. A.; Gresch, D.; Wang, Z. J.; Wu, Q. S.; Troyer, M.; Dai, X.; Bernevig, B. A. Type-II Weyl Semimetals. *Nature* **2015**, *527*, 495−498.

(16) Fu, L.; Wang, F.; Wu, B.; Wu, N.; Huang, W.; Wang, H.; Jin, C.; Zhuang, L.; He, J.; Fu, L.; Liu, Y. Q. Van der Waals Epitaxial Growth of Atomic Layered HfS_2 Crystals for Ultrasensitive Near-Infrared Phototransistors. *Adv. Mater.* **2017**, *29*, 1700439.

(17) Gao, Y.; Liu, Z.; Sun, D. M.; Huang, L.; Ma, L. P.; Yin, L. C.; Ma, T.; Zhang, Z.; Ma, X. L.; Peng, L. M.; Cheng, H. M.; Ren, W. C. Large-Area Synthesis of High-Quality and Uniform Monolayer WS_2 on Reusable Au Foils. *Nat. Commun.* **2015**, *6*, 8569.

(18) Gong, Y. J.; Ye, G. L.; Lei, S. D.; Shi, G.; He, Y. M.; Lin, J. H.; Zhang, X.; Vajtai, R.; Pantelides, S. T.; Zhou, W.; Li, B.; Ajayan, P. M. Synthesis of Millimeter-Scale Transition Metal Dichalcogenides Single Crystals. *Adv. Funct. Mater.* **2016**, *26*, 2009−2015.

(19) Tan, C.; Zhang, H. Epitaxial Growth of Hetero-Nanostructures Based on Ultrathin Two-Dimensional Nanosheets. *J. Am. Chem. Soc.* **2015**, *137*, 12162−12174.

(20) Lin, M.; Wu, D.; Zhou, Y.; Huang, W.; Jiang, W.; Zheng, W.; Zhao, S.; Jin, C.; Guo, Y.; Peng, H. L.; Liu, Z. F. Controlled Growth of Atomically Thin In_2Se_3 Flakes by van der Waals Epitaxy. *J. Am. Chem. Soc.* **2013**, *135*, 13274−13277.

(21) Ji, Q.; Zhang, Y.; Gao, T.; Zhang, Y.; Ma, D.; Liu, M.; Chen, Y.; Qiao, X.; Tan, P. H.; Kan, M.; Feng, J.; Sun, Q.; Liu, Z. F. Epitaxial Monolayer MoS_2 on Mica with Novel Photoluminescence. *Nano Lett.* **2013**, *13*, 3870−3877.

(22) Zhou, Y.; Nie, Y.; Liu, Y.; Yan, K.; Hong, J.; Jin, C.; Zhou, Y.; Yin, J.; Liu, Z.; Peng, H. L. Epitaxy and Photoresponse of Two-Dimensional GaSe Crystals on Flexible Transparent Mica Sheets. *ACS Nano* **2014**, *8*, 1485−1490.

(23) Cowley, R. The Lattice Dynamics of an Anharmonic Crystal. *Adv. Phys.* **1963**, *12*, 421−480.

(24) Lim, T.; Polanyi, J. C.; Guo, H.; Ji, W. Surface-Mediated Chain Reaction through Dissociative Attachment. *Nat. Chem.* **2011**, *3*, 85−89.

(25) Lim, T. B.; McNab, I. R.; Polanyi, J. C.; Guo, H.; Ji, W. Multiple Pathways of Dissociative Attachment: CH_3Br on Si(100)-2 × 1. *J. Am. Chem. Soc.* **2011**, *133*, 11534−11539.

(26) Acerce, M.; Voiry, D.; Chhowalla, M. Metallic 1T Phase MoS_2 Nanosheets as Supercapacitor Electrode Materials. *Nat. Nanotechnol.* **2015**, *10*, 313−318.

(27) Hu, J.; Liu, X.; Yue, C. L.; Liu, J. Y.; Zhu, H. W.; He, J. B.; Wei, J.; Mao, Z. Q.; Antipina, L. Y.; Popov, Z. I.; Sorokin, P. B.; Liu, T. J.; Adams, P. W.; Radmanesh, S. M. A.; Spinu, L.; Ji, H.; Natelson, D. Enhanced Electron Coherence in Atomically Thin Nb_3SiTe_6. *Nat. Phys.* **2015**, *11*, 471−477.

(28) Guo, G. Y.; Liang, W. Y. The Electronic Structures of Platinum Dichalcogenides: PtS_2, $PtSe_2$ and $PtTe_2$. *J. Phys. C: Solid State Phys.* **1986**, *19*, 995−1008.

(29) Chen, J.; Badioli, M.; Alonso-Gonzalez, P.; Thongrattanasiri, S.; Huth, F.; Osmond, J.; Spasenovic, M.; Centeno, A.; Pesquera, A.; Godignon, P.; Elorza, A. Z.; Camara, N.; Garcia de Abajo, F. J.; Hillenbrand, R.; Koppens, F. H. Optical Nano-Imaging of Gate-Tunable Graphene Plasmons. *Nature* **2012**, *487*, 77−81.

(30) Fei, Z.; Rodin, A. S.; Andreev, G. O.; Bao, W.; McLeod, A. S.; Wagner, M.; Zhang, L. M.; Zhao, Z.; Thiemens, M.; Dominguez, G.; Fogler, M. M.; Castro Neto, A. H.; Lau, C. N.; Keilmann, F.; Basov, D. N. Gate-Tuning of Graphene Plasmons Revealed by Infrared Nano-Imaging. *Nature* **2012**, *487*, 82−85.

(31) Fujita, M.; Wakabayashi, K.; Nakada, K.; Kusakabe, K. Peculiar Localized State at Zigzag Graphite Edge. *J. Phys. Soc. Jpn.* **1996**, *65*, 1920−1923.

(32) Jablan, M.; Buljan, H.; Soljacic, M. Plasmonics in Graphene at Infrared Frequencies. *Phys. Rev. B: Condens. Matter Mater. Phys.* **2009**, *80*, 245435.

(33) Zhang, W. X.; Huang, Z. S.; Zhang, W. L.; Li, Y. R. Two-Dimensional Semiconductors with Possible High Room Temperature Mobility. *Nano Res.* **2014**, *7*, 1731−1737.

(34) Chen, K.; Chen, Z.; Wan, X.; Zheng, Z.; Xie, F.; Chen, W.; Gui, X.; Chen, H.; Xie, W.; Xu, J. A Simple Method for Synthesis of High-Quality Millimeter-Scale 1T' Transition-Metal Telluride and Near-Field Nanooptical Properties. *Adv. Mater.* **2017**, *29*, 1700704.

Supporting Information

Highly Organized Epitaxy of Dirac Semimetallic $PtTe_2$ Crystals with Extrahigh Conductivity and Visible Surface Plasmons at Edges

Lei Fu, [†,‡] *Debo Hu,* [‖] *Rafael G. Mendes,* [§] *Mark H. Rümmeli,* [§] *Qing Dai,* [‖] *Bin Wu,* [‡,*] *Lei Fu,* [†,*] *and Yunqi Liu* [‡,*]

[†]College of Chemistry and Molecular Science, Wuhan University, Wuhan 430072, P. R. China

[‡]Beijing National Laboratory for Molecular Sciences, Key Laboratory of Organic Solids, Institute of Chemistry, Chinese Academy of Science, Beijing 100190, P. R. China

[§]Soochow Institute for Energy and Materials InnovationS (SIEMIS), School of Energy Optoelectronics and Energy & Collaborative Innovation Center of Suzhou Nano Science and Technology, Soochow University, Suzhou 215006, P. R. China

[‖]National Center for Nanoscience and Technology, Beijing 100190, China

Corresponding Author

wubin@iccas.ac.cn, leifu@whu.edu.cn, liuyq@iccas.ac.cn

DFT calculations: The CASTEP module of Materials Studio software was used in the DFT calculations on energy of all structures.[1] The ultrasoft pseudopotentials were used to represent the interactions between the ionic cores and the valence electrons. The plane-wave basis set cut-off energy was fixed at 300 eV in all calculations after convergence test. Brillouin-zone sampling was performed on Monkhorst–Pack special points using a Methfessel–Paxton integration scheme with 4 × 4 × 4 mesh. The geometry optimization was achieved under the Broyden–Fletcher–Goldfarb–Shanno minimization scheme. The crystal structures, including lattice constants and internal atomic coordinates, were optimized independently to minimize the free enthalpy, interatomic forces and stresses of the unit cell. The tolerances for geometrical optimization were: differences for total energy within 10^{-5} eV/atom, maximum ionic Hellmann–Feynman force[2] within 0.03 eV/Å, maximum ionic displacement within 0.001 Å, and maximum stress within 0.05 GPa. For surface calculations, periodic 2 × 2 × 1 supercells containing a finite slab and a 10 Å vacuum layer was used to prevent interactions between periodic atoms.

The calculated adsorption energies are defined as follows:

$$E_a = E_{total} - (E_{surface} + E_{molecule})$$

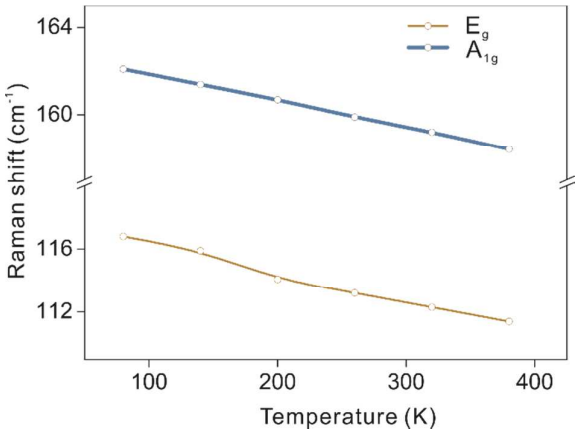

Figure S1. Corresponding linear temperature coefficients (X) of E_g and A_{1g} Raman modes plotted as a function of testing temperature.

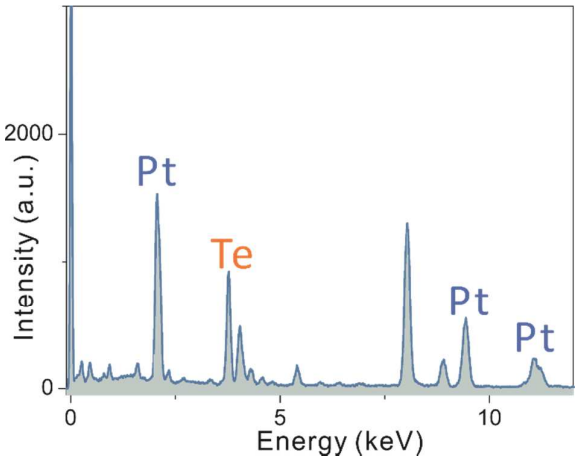

Figure S2. The TEM-EDS survey spectrum of the $PtTe_2$ in Figure 2c.

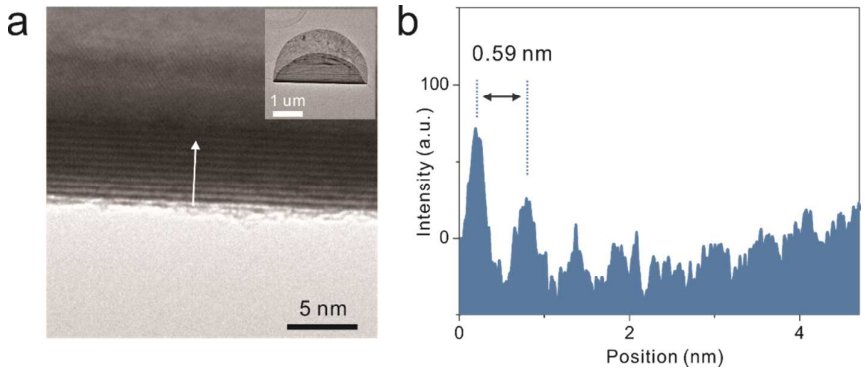

Figure S3. (a) Zoomed-in TEM image of the folded edge of the $PtTe_2$ crystal (with the TEM image shown in the inset). Inset: low-magnification TEM image captured on a folded edge of a $PtTe_2$ crystal. (b) Intensity line profile (blue line) of the white dashed arrow in (a).

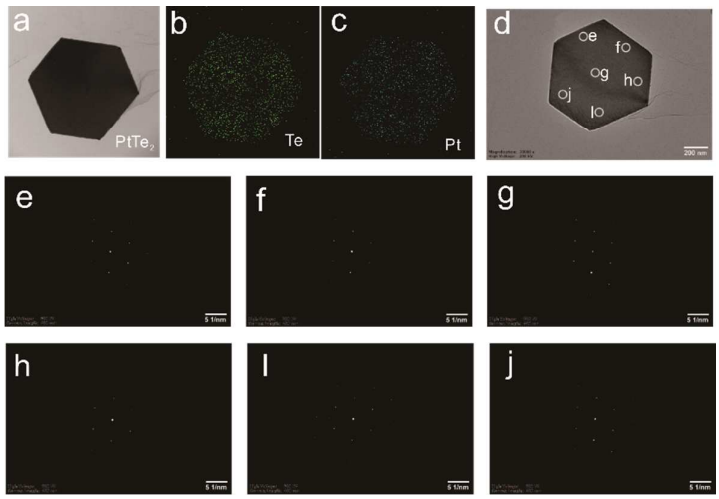

Figure S4. (a, d) Low-magnification TEM image of a hexagonal $PtTe_2$ crystal. (b, c) EDS elemental mapping of Te–L, Pt–M of the hexagonal $PtTe_2$ crystal in (a), respectively. (e–j) SAED pattern from the selected area of the hexagonal crystal in (d).

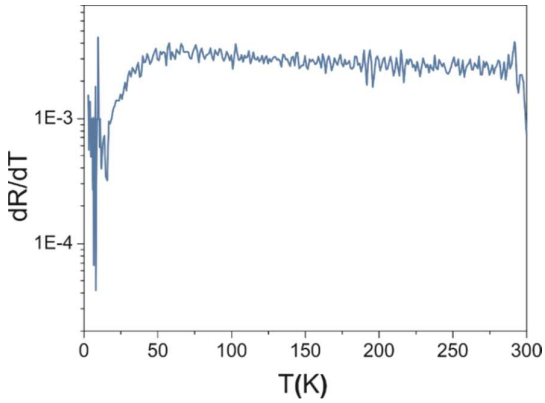

Figure S5. dR/dT–T curves of a 9 nm $PtTe_2$ crystal device.

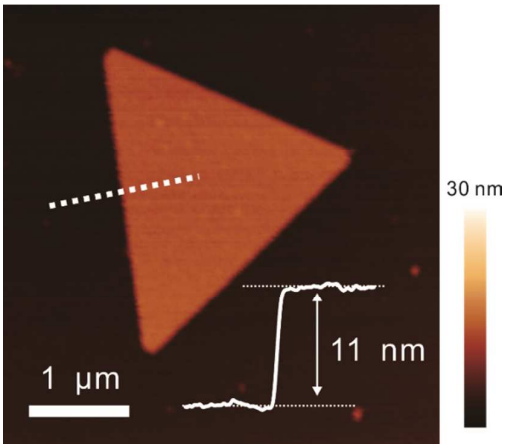

Figure S6. AFM topographic image of a 11 nm $PtTe_2$ crystal in Figure 5e.

REFERENCES

(1) Perdew, J. P.; Burke, K.; Ernzerhof, M. Generalized Gradient Approximation Made Simple. *Phys. Rev. Lett.* **1996**, *77*, 3865.

(2) Press, W. H.; Flannery, B. P.; Teukolsky, S. A.; Vetterling, W. T. Numerical Recipes in C (Cambridge University Press, New York, 1986).